

# Removal of Elemental Mercury from Flue Gas using the Magnetic Attapulgite by Mn-Cu Oxides Modification

**Yifei Long**

Wuhan University

**Zhong He**

Wuhan University

**Xiaoyi Li**

Wuhan University

**Yajie Yin**

Wuhan University

**Yuan Wang**

Wuhan University

**Honghu Li**

Wuhan University

**Jiangjun Hu** (✉ [jjhu1963@outlook.com](mailto:jjhu1963@outlook.com))

Wuhan University

---

## Research Article

**Keywords:** Mercury, Attapulgite, Manganese, Copper, Coal-fired flue gas

**Posted Date:** May 26th, 2021

**DOI:** <https://doi.org/10.21203/rs.3.rs-497732/v1>

**License:**   This work is licensed under a Creative Commons Attribution 4.0 International License.

[Read Full License](#)

---

**Version of Record:** A version of this preprint was published at Environmental Science and Pollution Research on October 2nd, 2021. See the published version at <https://doi.org/10.1007/s11356-021-16777-z>.

# Abstract

Mercury pollution has become one of the most concerned environmental issues in the world because of its high toxicity, non-degradability and bioaccumulation. Attapulgite adsorbents modified by magnetic manganese-copper ( $Mn_xCu_y$ -MATP) were fabricated by co-precipitation and ultrasonic impregnation method, aiming at removing  $Hg^0$  from coal-fired flue gas. BET, SEM, XRD, VSM and XPS were used to systematically explore the physical and chemical properties of the adsorbents, the effects of manganese and copper additions, reaction temperature and various components in the flue gas on the efficiency of  $Hg^0$  removal were investigated.  $Mn_8Cu_5$ -MATP exhibited the optimal properties, and excessive copper loadings led to the aggregation of the active components. The efficiency of mercury removal can be effectively improved by NO and HCl regardless of the absence and presence of  $O_2$ , because the  $NO^+$ ,  $NO_3$ ,  $NO_2$  and  $Cl^*$  produced during the reaction can promote the adsorption and oxidation of  $Hg^0$ .  $SO_2$  and  $H_2O$  inhibited the oxidation of  $Hg^0$  because of the competitive adsorption at the active sites, while a large amount of sulfite and sulfate were formed to block the pores. However, the introduction of copper caused the sample to obtain  $SO_2$  resistance, which resulted in a mercury removal efficiency of 84.3% even under 1500 ppm  $SO_2$ . In addition, after 5 cycles of adsorption and regeneration,  $Mn_8Cu_5$ -MATP can still maintain excellent  $Hg^0$  removal ability. The fabricated adsorbent can save the actual production cost and effectively improve the mercury removal efficiency in sulfur-containing flue gas.

## 1. Introduction

Mercury has attracted widespread public attention due to its high toxicity, persistence, high volatility, and bioaccumulation (Li et al. 2017a, Wang et al. 2019a, Yang et al. 2020b). In recent years, mercury in coal-fired flue gas has been considered the main source of mercury pollution (Zhao et al. 2019). Therefore, it is necessary to control mercury emissions in coal-fired flue gas. Generally, mercury in coal-fired flue gas is divided into three categories, including elemental mercury ( $Hg^0$ ), divalent mercury ( $Hg^{2+}$ ) and particulate mercury ( $Hg^p$ ) (Wilcox et al. 2012, Xu et al. 2014). Among them,  $Hg^{2+}$  and  $Hg^p$  can be effectively removed by the wet desulfurization and particulate matter control devices (Yang et al. 2019b). However,  $Hg^0$  cannot be easily removed due to its chemical stability (Yang et al. 2019a). Therefore, it is urgent to develop a technology for removal  $Hg^0$ .

At present, a variety of mercury removal methods have been proposed by researchers, such as chemical adsorption, photocatalytic oxidation and thermal catalytic oxidation (Jia et al. 2020, Wu et al. 2017, Zhang et al. 2019). Among them, the flue injection technology of mercury removal adsorbent is validated to be a practical and feasible mercury removal technology (Chen et al. 2019). Activated carbon adsorbent has become a research hotspot in the field of mercury removal from flue gas owing to its excellent adsorption performance (Huang et al. 2019). However, the activated carbon injection technology is not only expensive, but also cannot be recycled, which impedes its practical application (Yang et al. 2019d). In addition, the pollution of fly ash has a negative impact on the resource utilization due to the

incorporation of activated carbon containing mercury (Zhao et al. 2017). More importantly, such technology cannot achieve the ultimate centralized control for mercury pollution in coal-fired flue gas. Instead, the mercury and its compounds in the flue gas were transferred to by-products such as fly ash, desulfurization slurry, and desulfurization gypsum through activated carbon, which increases the risk of environmental pollution caused by the secondary release of mercury (Wang et al. 2020). In order to avoid the risk, researchers consider incorporating magnetic materials into the adsorbent to achieve the purpose of separating the adsorbent from fly ash (Dong et al. 2009, Yang et al. 2018a, Zhou et al. 2019). Bordedeux et al. prepared nano-Fe<sub>2</sub>O<sub>3</sub> with high specific surface area for Hg<sup>0</sup> removal (Borderieux et al. 2004). The mercury absorption capacity can reach 1390 µg/g at the optimal reaction temperature of 260°C. Yang et al. developed a magnetic nano (Fe<sub>3-x</sub>Mn<sub>x</sub>)<sub>1-δ</sub>O<sub>4</sub> adsorbent, which showed excellent mercury adsorption performance at 100–300°C (Yang et al. 2011). Yang et al. successfully synthesized a magnetic activated carbon for Hg<sup>0</sup> removal by co-precipitation method, and the mercury removal performance was optimal when the mass fraction of magnetic substance was 25% (Yang et al. 2020a). Although these magnetic adsorbents can effectively remove mercury and regenerate, the synthesis process is usually complex and costly. In order to develop cheaper adsorbents, researchers have focused on natural minerals (Ding et al. 2012, Li et al. 2014, Liu et al. 2020, Shao et al. 2016). Among a variety of natural minerals, attapulgite (ATP) has attracted much attention due to its nano-scale rod-like structure, excellent thermal stability and large surface area (Liu et al. 2017). Liu et al. modified ATP with MnO<sub>2</sub> and Co<sub>3</sub>O<sub>4</sub>, which greatly improved the efficiency of mercury removal (Liu et al. 2014). Huang et al. prepared a magnetic manganese-modified ATP, which exhibited good mercury removal and regeneration performance (Dong et al. 2021).

Although these adsorbents show good mercury removal capacity and regeneration performance, the mercury removal efficiency of adsorbents reduces greatly under SO<sub>2</sub> long-term operation, which limits their further development and application (Dong et al. 2019). In order to alleviate above negative effect, we simultaneously loaded Mn-Cu into magnetic ATP by ultrasonic impregnation, and evaluated Hg<sup>0</sup> removal efficiency under different conditions. The physicochemical properties of the adsorbent were systematically analyzed by XRD, SEM, BET, VSM, XPS. The effects of manganese and copper additions, reaction temperature and various components in the flue gas on the efficiency of Hg<sup>0</sup> removal were investigated. In addition, the regeneration performance of the adsorbent was also tested. The prepared adsorbent possessed high mercury removal efficiency, and exhibits excellent SO<sub>2</sub> resistance. The results of this work can provide valuable guidance for the development of mercury removal adsorbents with SO<sub>2</sub> resistance.

## 2. Experimental

### 2.1 Adsorbent preparation

MATP: The raw attapulgite (ATP) was purchased from Yixiang New Materials Co., Ltd. The ATP was first washed with deionized water to remove soluble impurities on the surface. Then, the pre-treated ATP was

added into the aqueous solution containing  $\text{FeCl}_3$  and  $\text{FeCl}_2$ . The mass ratio of the ATP:  $\text{FeCl}_3$ :  $\text{FeCl}_2$  was 3.66: 2.57: 1. Subsequently, concentrated ammonia was added to the ATP suspension during the stirring process until the pH value reached approximately 11. Further, the suspension was stirred at  $70^\circ\text{C}$  for 90 min, after which the obtained sediment was washed to neutrality and dried at  $105^\circ\text{C}$  for 12 h. Finally, the sample was calcined at  $250^\circ\text{C}$  for 3h under  $\text{N}_2$  atmosphere to obtain the MATP.

$\text{Mn}_x$ -MATP and  $\text{Mn}_x\text{Cu}_y$ -MATP: The MATP was immersed in a calculated amount of 50wt%  $\text{Mn}(\text{NO}_3)_2$  solution (and  $\text{Cu}(\text{NO}_3)_2$  solution), and then the mixture was exposed to an ultrasonic bath at  $60^\circ\text{C}$  for 2 h. Subsequently, the obtained powder was dried at  $105^\circ\text{C}$  for 12 h, and calcined at  $450^\circ\text{C}$  for 4h under  $\text{N}_2$  atmosphere with a temperature rise rate of  $7.5^\circ\text{C}/\text{min}$ . The obtained samples were represented by  $\text{Mn}_x$ -MATP or  $\text{Mn}_x\text{Cu}_y$ -MATP, where x and y represented the mass percent of element Mn and Cu on the samples, respectively.

## 2.2 Adsorbent characterization

The specific surface areas and the pore size distributions of the adsorbent were analyzed on an ASAP 2020 analyzer (Micromeritics Inc., USA) using  $\text{N}_2$  gas as an adsorbate at liquid-nitrogen temperature (77 K). The phase structure of the adsorbent was characterized by X-ray diffraction (XRD). The XRD pattern was recorded on a D/MX-III A diffractometer (Rigaku, Japan) with Ni-filtered Cu K $\alpha$  radiation. The scanning range was set from  $5^\circ$  to  $90^\circ$  ( $2\theta$ ) with a step size of  $0.02^\circ$  and a step time of 2 min. The magnetism of the adsorbent was characterized by using a physical property measurement system using a VSM (LakeShore7404). The surface composition and the chemical state of the elements existing in the adsorbent were analyzed on a Thermo ESCALAB 250Xi apparatus using Al K $\alpha$  radiation as the excitation source and the binding energies were referenced to the C1s at 284.8 eV.

## 2.3 Measurement of $\text{Hg}^0$ adsorption performance

The mercury adsorption performance of the adsorbent was tested on a laboratory-scale fixed bed adsorption system, as shown in Fig. 1. The gas compositions were  $\text{N}_2$ ,  $\text{O}_2$ ,  $\text{NO}$ ,  $\text{SO}_2$ ,  $\text{HCl}$ ,  $\text{Hg}^0$  vapor and  $\text{H}_2\text{O}$  vapor. The  $\text{Hg}^0$  concentration was maintained at approximately  $55 \mu\text{g}/\text{m}^3$  by adjusting  $\text{N}_2$  to flow through the mercury permeation tube (HE-SR, VICI Metronics, USA) and oil bath temperature.  $\text{Hg}^0$  capture experiments were performed in a quartz tube reactor (internal diameter was 7 mm) in the fixed bed reactor. During the experiment, the sample was fixed in the middle of the quartz tube reactor by quartz wool, while the quartz tube reactor was wrapped in a temperature-programmed tube furnace. A total of 50 mg of the prepared samples were used for each experiment. A total gas flow rate was controlled at 1 L/min, which resulted in a GHSV of approximately 400,000 h $^{-1}$ . All the gas pipes after the oil bath were heated by electric heating tapes to ensure a stable temperature of  $90^\circ\text{C}$  for the purpose of preventing the deposition of Hg. A mercury analyzer (AFS-930, Beijing Titan Instruments Co., Ltd.) was utilized to detect the  $\text{Hg}^0$  concentration at the inlet and outlet of the quartz tube reactor. The  $\text{Hg}^0$  removal efficiency ( $\eta$ ) of the reaction was calculated by the formulas as follows:

$$\eta (\%) = (1 - [\text{Hg}^0]_{\text{out}} / [\text{Hg}^0]_{\text{in}}) \times 100\%. \quad (1)$$

where  $[\text{Hg}^0]_{\text{in}}$  and  $[\text{Hg}^0]_{\text{out}}$  represented the  $\text{Hg}^0$  concentration at the inlet and outlet of reaction. Sampling tests and analyses were performed in triplicates to minimize the error and uncertainty.

## 3. Results And Discussion

### 3.1. Sample Characterization

The crystal phases of MATP and  $\text{Mn}_8\text{Cu}_y\text{-MATP}$  samples were determined by XRD analysis, as shown in Fig. 2. After magnetic modification, distinct diffraction peaks were observed at  $30.233^\circ$ ,  $35.576^\circ$ ,  $37.214^\circ$ ,  $43.207^\circ$ ,  $53.606^\circ$ ,  $57.132^\circ$  and  $62.722^\circ$ , corresponding to magnetic  $\text{Fe}_3\text{O}_4$  (PDF 75 – 0033) particles (Xu et al. 2019). This phenomenon indicated that the magnetic component had been successfully loaded onto the ATP surface. After introducing the elements Mn and Cu, peaks were observed at  $2\theta$  values of  $30.118^\circ$ ,  $35.485^\circ$ ,  $37.169^\circ$ ,  $43.176^\circ$ ,  $53.639^\circ$ ,  $57.137^\circ$  and  $62.786^\circ$ , corresponding to  $\text{Mn}_3\text{O}_4$  (PDF 13–0162) (Liu et al. 2018). The peak intensity was slightly increased due to the high overlap of the diffraction peaks of  $\text{Mn}_3\text{O}_4$  with  $\text{Fe}_3\text{O}_4$ . Besides, this phenomenon may also be ascribed to the increase of  $\text{Fe}_3\text{O}_4$  crystallinity caused by introducing manganese and copper oxides. In addition, the diffraction peaks associated with  $\text{MnO}_2$  were not observed, which can be attributed to the existence of amorphous phase (Shan et al. 2019). The diffraction peaks at  $36.512^\circ$ ,  $42.401^\circ$  and  $61.471^\circ$  belonged to  $\text{Cu}_2\text{O}$  (PDF 65-3288) were observed, while the distinct reflection at  $35.477^\circ$  and  $38.560^\circ$  could be ascribed to  $\text{CuO}$  (PDF 48-1548) (Hosseini et al. 2014). This phenomenon elucidated that the  $\text{Cu}_2\text{O}$  and  $\text{CuO}$  coexisted on the sample. As the content of Cu increased, the diffraction peak of  $\text{Mn}_3\text{O}_4$  decreased imperceptibly, which can be ascribed to a synergistic effect between copper and manganese oxides, thereby preventing manganese oxides from reaching the crystal structure. Such the synergistic effect can improve the oxygen vacancies and presumably the high catalytic activity (Cao et al. 2012). However, the crystallinity increased slightly when the Cu content was greater than 5, which reflected that the excessive  $\text{CuO}_x$  was not conducive to the dispersion of Mn species.

The surface morphology of the original ATP, MATP and  $\text{Mn}_8\text{Cu}_y\text{-MATP}$  were investigated by FE-SEM. As shown in Fig. 3a, it can be clearly seen that the original ATP contained a smooth rod-like morphology, which facilitates the formation of metal oxide particles on the surface (Zhang et al. 2014). After the magnetic modification, some small particles appeared on the surface of ATP, denoting the successful loading of the magnetic substance (Fig. 3b). As exhibited in Fig. 3c-g, more particles were formed on the surface after introducing copper and manganese oxides. In addition, the particles on the surface gradually increased and dispersed more uniformly with the increasing of Cu content, which was attributed to the interaction between copper and manganese oxides. Nevertheless, the agglomeration phenomenon was extremely obvious on the surface when the Cu content was greater than 5 (Fig. 3h), which inhibited the activity of the sample to a certain extent. These results were consistent with the aforementioned XRD results.

Table 1  
BET characterization results for different metal loading catalysts.

<b>Samples</b>	<b>BET surface area (m<sup>2</sup>g<sup>-1</sup>)</b>	<b>Pore Volume (cm<sup>3</sup>g<sup>-1</sup>)</b>	<b>Average pore diameter (nm)</b>
MATP	127.51	0.1776	9.633
Mn <sub>8</sub> -MATP	96.93	0.2340	10.894
Mn <sub>8</sub> Cu <sub>1</sub> -MATP	107.36	0.2332	8.688
Mn <sub>8</sub> Cu <sub>2</sub> -MATP	106.23	0.2539	9.060
Mn <sub>8</sub> Cu <sub>3</sub> -MATP	105.19	0.2382	9.256
Mn <sub>8</sub> Cu <sub>4</sub> -MATP	100.84	0.2411	9.460
Mn <sub>8</sub> Cu <sub>5</sub> -MATP	101.98	0.2395	9.542
Mn <sub>8</sub> Cu <sub>6</sub> -MATP	77.44	0.1696	8.761

The overall microstructure characteristics of the prepared samples were characterized by BET, as elaborated in Table 1. After modified by manganese, the specific surface area of the sample decreased while the pore volume and average pore diameter increased slightly. This phenomenon may be caused by manganese oxide entering the inner surface of the MATP, blocking part of the pores. After introducing copper, the specific surface area of the samples were higher than the MATP modified by manganese except for Mn<sub>8</sub>Cu<sub>6</sub>-MATP, which revealed that the synergistic effect between copper and manganese oxides was beneficial to the increase of BET surface area (Yi et al. 2017). However, the surface area was decayed with increasing the content of Cu except for Mn<sub>8</sub>Cu<sub>4</sub>-MATP, which may be related to the blockage of a few pores caused by the increase in the total load. Moreover, such the decay trend of the surface area became more pronounced as the load increased. When the Cu content reached 6, the specific surface area was significantly decreased by the substantial agglomeration of the active components, which was in line with the SEM results. In addition, the MATP modified by manganese and copper possessed smaller average pore diameter and higher pore volume than the original MATP. Such phenomenon can be attributed to the removal of volatiles during the ultrasonic impregnation and calcination process as well as the chaotic accumulation of loaded active components, resulting in the formation of some new pores (Wang et al. 2016). Combined with SEM and BET, Mn<sub>8</sub>Cu<sub>5</sub>-MATP can provide a larger active surface area, leading to strong interactions, which was beneficial to the adsorption and catalytic oxidation of mercury.

Magnetism is an important factor in determining whether the adsorbent can be separated and recycled. Therefore, the magnetization of the samples was investigated by using the VSM (LakeShore7404) and the results were presented in Fig. 4. After modified by manganese, a slight decline of saturation magnetization was observed, from 17.78 emu/g to 16.46 emu/g, reflecting that the loading of

manganese had a slight effect on the saturation magnetization. This phenomenon may be related to the increase in the crystallinity of  $\text{Fe}_3\text{O}_4$  by the addition of manganese, which was consistent with the aforementioned XRD and SEM results. Notably, the influence of introducing copper towards the saturation magnetization was negligible, which changed from 16.46 emu/g to 16.02 emu/g. In addition, magnetization hysteresis and coercivity of the three samples were not observed, which suggested that they are superparamagnetic adsorbents. After tests, the three adsorbents can be separated from fly ash through an external magnets.

XPS analysis was usually utilized to elucidate the composition of different species and the element valence states on the samples. Thus, the chemical states of the fresh adsorbent was investigated, and the XPS spectra of Mn 2p, Fe 2p, Cu 2p and O 1s regions were obtained, as elaborated in Fig. 5. As seen from the XPS spectra of Fe 2p (Fig. 5a), three peaks in a range from 705 eV to 730 eV corresponded to Fe  $2p_{3/2}$ , shake-up satellite and Fe  $2p_{1/2}$ , respectively. Moreover, the Fe  $2p_{3/2}$  spectra can be divided by deconvolution into three peaks at 709.6 eV, 710.9 eV and 713.0 eV (Zhang et al. 2018). Among them, the peaks at 710.9 eV and 713.0 eV were assigned to the  $\text{Fe}^{3+}$  in octahedral and tetrahedral coordination, respectively, while the peak at 709.6 eV corresponded to  $\text{Fe}^{2+}$  (Chen et al. 2014). As shown in Table 2,  $\text{Fe}^{3+}$  on the sample after mercury removal was 4.27% lower than that before the reaction, which indicated that some  $\text{Fe}^{3+}$  on the surface was reduced to  $\text{Fe}^{2+}$  during the oxidization of  $\text{Hg}^0$ . As for the Mn 2p spectra in Fig. 5b, two main peaks at 641.6 eV and 653.0 eV were observed, corresponding to Mn  $2p_{3/2}$  and Mn  $2p_{1/2}$ , respectively. In addition, the shake-up satellite was observed at 647.5 eV. The Mn  $2p_{3/2}$  spectra can be separated into three peaks, which were corresponded to  $\text{Mn}^{4+}$  (643.5 eV),  $\text{Mn}^{3+}$  (641.9 eV) and  $\text{Mn}^{2+}$  (640.7 eV) (Feng et al. 2017, Yang et al. 2018a). Combined with the result that the crystal phase diffraction peaks related to  $\text{MnO}_2$  were not observed in the XRD pattern, it is further confirmed that  $\text{MnO}_2$  was present in the adsorbent with amorphous phase. After mercury removal, the contents of  $\text{Mn}^{4+}$  and  $\text{Mn}^{3+}$  decreased in varying degrees, from 29.18% and 34.09–25.49% and 32.17%, respectively, while  $\text{Mn}^{2+}$  increased significantly. This phenomenon was attributed to the fact that  $\text{Mn}^{4+}$  can directly oxidize  $\text{Hg}^0$  to  $\text{Hg}^{2+}$ . In addition,  $\text{Mn}^{3+}$  can also participate in the oxidation of  $\text{Hg}^0$  under oxygen-containing conditions. The XPS spectra of Cu 2p was depicted in Fig. 5c, it can be seen obviously that two main peaks at 933.4 eV and 953.0 eV corresponded to Cu  $2p_{3/2}$  and Cu  $2p_{1/2}$ , respectively, and two satellite peaks (962.1 eV and 942.1 eV). The two main peaks can be fitted into two peaks, of which Cu 2p with asymmetric characteristics at 932.6 eV and 952.5 eV was  $\text{Cu}^+$ , while  $\text{Cu}^{2+}$  appeared at 934.3 eV and 953.7eV, accompanying with two shake-up satellites (Wang et al. 2019b). According to previous reports,  $\text{Cu}_2\text{O}$  was a p-type semiconductor catalyst with hole conduction capacity and preferentially adsorbing  $\text{O}_2$ , which led to a higher catalytic oxidation activity (Bao et al. 2014, Zhang et al. 2020). Moreover, more oxygen vacancies can be formed through the interaction between  $\text{Mn}^{4+}/\text{Mn}^{3+}/\text{Mn}^{2+}$  and  $\text{Cu}^{2+}/\text{Cu}^+$  ( $\text{Mn}^{4+}/\text{Mn}^{3+} + \text{Cu}^+ \rightarrow \text{Mn}^{2+} + \text{Cu}^{2+}$ ), thereby further improving the mercury removal efficiency (Yang et al. 2019c, Yang et al. 2018b). As exhibited in Fig. 5d, the O 1s peak was divided into three peaks at 529.6 eV, 531.7 eV, and 532.6 eV, corresponding to the lattice oxygen in metal oxides ( $\text{O}_A$ ), chemisorbed oxygen ( $\text{O}_B$ ) and oxygen

in hydroxyl-like groups ( $O_C$ ), respectively (Zhang et al. 2017). It can be seen that the content of  $O_B$  was significantly reduced after the reaction, confirming that  $O_B$  had been consumed.

Table 2  
Surface element compositions detected by XPS.

Sample	Fe <sup>3+</sup>	Fe <sup>2+</sup>	Mn <sup>4+</sup>	Mn <sup>3+</sup>	Mn <sup>2+</sup>	Cu <sup>2+</sup>	Cu <sup>+</sup>	O <sub>A</sub>	O <sub>B</sub>
Fresh Mn <sub>8</sub> Cu <sub>5</sub> -MATP	83.46	16.54	29.18	34.09	36.73	55.62	44.38	10.73	74.68
Used Mn <sub>8</sub> Cu <sub>5</sub> -MATP	79.19	20.81	25.49	32.17	42.33	50.97	49.03	15.44	68.91

### 3.2 Effect of manganese and copper loading

The mercury removal performance of the MATP with different manganese loadings was investigated at 100–300°C to determine the best manganese content. As seen from Fig. 6a, it was clearly observed that the mercury removal efficiency of the five samples increased at first and then decreased with the reaction temperature increasing. Among them, four kinds of adsorbents containing manganese reached the highest mercury removal efficiency at 150°C. In general, the increase of reaction temperature was beneficial to increase the molecular kinetic energy of reactants, thus promoting the catalytic oxidation of Hg<sup>0</sup>. Nevertheless, the excessive high reaction temperature can inhibit the adsorption process of Hg<sup>0</sup> on the adsorbent surface, resulting in the reduction of Hg<sup>0</sup> removal efficiency. Additionally, the mercury removal efficiency enhanced with the increase of manganese loading. The mercury removal efficiency reached the highest when the Mn loading increased to 8%. However, the mercury removal efficiency remained relatively constant although the manganese loading further increased to 10%. Such phenomenon can be attributed to the growth of crystalline size and surface blocking caused by excessive manganese loading (Kim et al. 2014). Hence, the Mn<sub>8</sub>-MATP was selected as the best manganese loading sample for consideration of actual cost and mercury removal efficiency.

Figure 6b showed the effect of different copper loadings on the mercury removal performance of the adsorbent. It can be clearly observed that the mercury removal efficiency of all adsorbents first increased and then decreased with increasing temperature. The mercury removal efficiency reached the maximum at 150°C. Moreover, the mercury removal efficiency of all adsorbents after the introduction of copper was higher than that before, which indicated that the synergy between copper and manganese oxides was beneficial to improve the mercury removal efficiency. In addition, the mercury removal efficiency improved with the increase of copper loading until the copper loading reached 5%. However, the mercury removal efficiency was significantly reduced when the copper loading further increased to 6%. This phenomenon can be attributed to the blockage of a large number of pores caused by excessive metal oxides, which was consistent with the BET result. Therefore, combined with a series of characterization results mentioned above, Mn<sub>8</sub>Cu<sub>5</sub>-MATP possessed the unique microstructure, larger specific surface area, more active sites and stronger oxygen migration ability, which was beneficial to mercury removal.

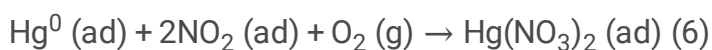
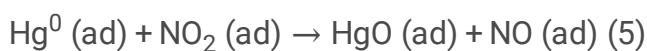
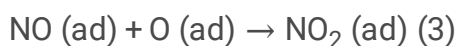
## 3.3 Effect of individual flue gas components

### 3.3.1. Effect of O<sub>2</sub>

O<sub>2</sub> is one of the key factors affecting the efficiency of mercury removal. As shown in Fig. 7, the effect of different O<sub>2</sub> concentrations in the simulated flue gas on the efficiency of mercury removal at 150°C was investigated. It can be obviously seen that the mercury removal efficiency was 81.1% despite absence of O<sub>2</sub>, which was due to the consumption of a large amount of O<sub>A</sub> and O<sub>B</sub>. When the O<sub>2</sub> concentration improved from 0–6%, the mercury removal efficiency significantly increased to 91.1%, which can be ascribed to the regeneration of O<sub>A</sub> and O<sub>B</sub> consumed during the removal process and the replenishment of gas-phase oxygen (Chen et al. 2018). Nevertheless, the improvement of mercury removal efficiency was negligible when the O<sub>2</sub> concentration further increased to 9%, which denoted that 6% O<sub>2</sub> was sufficient to complete the oxidation of Hg<sup>0</sup>.

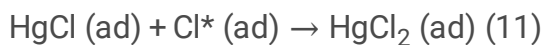
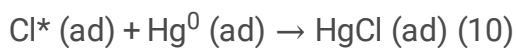
### 3.3.2. Effect of NO

As an inherent component of coal-fired flue gas, NO is usually approximately 4 orders of magnitude higher than the concentration of mercury, which has an important effect on the oxidation of Hg<sup>0</sup>. As described in Fig. 8, the effect of NO on the efficiency of mercury removal under different conditions was investigated. The efficiency of mercury removal under 500 ppm NO without O<sub>2</sub> was greatly improved compared with the pure N<sub>2</sub> atmosphere. Moreover, the mercury removal efficiency was further improved from 94.5–98.4% after the addition of 6% O<sub>2</sub>. This result demonstrated that the mercury removal can be greatly promoted by NO with or without O<sub>2</sub>, which was similar to previous reports (Li et al. 2012). However, the change in the removal efficiency of mercury was negligible when the concentration of NO was further increased to 1000 ppm, because 500 ppm NO was sufficient to oxidize mercury. The strong promoting effect of NO on mercury removal was attributed to the reaction of NO with reactive oxygen species on the surface of the adsorbent to form NO<sup>+</sup>, NO<sup>3-</sup> and NO<sub>2</sub>, which promoted the oxidation of mercury. The involved mechanisms can be explained by the following reactions (Shan et al. 2019):



### 3.3.3. Effect of HCl

Generally, there is a certain amount of chlorine in the coal, thus the HCl produced during the combustion process possesses a significant effect on the Hg<sup>0</sup> oxidation. It can be observed from Fig. 9 that the mercury removal efficiency can be promoted by HCl regardless of the absence and presence of O<sub>2</sub>. The mercury removal efficiency was increased from 81.0–90.9% when 10 ppm HCl was introduced in the pure N<sub>2</sub> atmosphere, whereas the increment was negligible when the concentration of HCl was increased to 20 ppm. Nevertheless, the mercury removal efficiency was further improved to 96.5% and 98.2% after adding 6% O<sub>2</sub> under the conditions of 10 and 20 ppm HCl, respectively. These phenomena elucidated that the oxidation of Hg<sup>0</sup> can be facilitated greatly by HCl, which can be explained by the Langmuir-Hinshelwood mechanism (Li et al. 2011). HCl is first adsorbed on the surface of the adsorbent and reacts with active oxygen to obtain active chlorine, and then further reacts with adsorbed Hg<sup>0</sup> to form HgCl<sub>2</sub>. The detailed reaction mechanisms are as follows (Hou et al. 2014):



### 3.3.4. Effect of SO<sub>2</sub> and H<sub>2</sub>O

As an inherent component of coal-fired flue gas, SO<sub>2</sub> usually inhibits the Hg<sup>0</sup> removal efficiency. Therefore, the effect of SO<sub>2</sub> towards Hg<sup>0</sup> removal efficiency under the condition of 6% O<sub>2</sub> was investigated, as presented in Fig. 10a. After introducing 500 ppm SO<sub>2</sub>, the removal efficiency of Hg<sup>0</sup> was almost unchanged, because SO<sub>2</sub> was oxidized to SO<sub>3</sub> by O<sub>2</sub> and further reacted with Hg<sup>0</sup> to form HgSO<sub>4</sub> (Tao et al. 2012). This reaction mechanism enabled a certain concentration of SO<sub>2</sub> to promote the oxidation of mercury, thus counteracting the negative effects. However, with the increase of SO<sub>2</sub> concentration to 1000 ppm and 1500 ppm, the Hg<sup>0</sup> removal efficiency decreased to 87.1% and 84.3%, respectively. Such inhibition phenomenon can be ascribed to a competitive adsorption at the active sites between SO<sub>2</sub> and Hg<sup>0</sup>, and the inhibition effect was far greater than the promotion effect (Xu et al. 2017). Moreover, the binding capacity of SO<sub>2</sub> to the active sites was stronger than that of Hg<sup>0</sup>. On the other hand, plenty of sulfites and sulfates were obtained through the reaction of SO<sub>2</sub> with metal oxides, which not only consumed the active sites but also blocked the pores for mercury removal (Chen et al. 2017). Interestingly, the inhibitory effect was weakened after the adding copper compared with the previously reports because copper oxides reacted with SO<sub>2</sub> preferentially and protect the active sites from poisoning, resulting in a certain SO<sub>2</sub> resistance (Dong et al. 2021). In addition, the effect of H<sub>2</sub>O on the efficiency of mercury removal was also evaluated, as reflected in Fig. 10b. As the concentration of H<sub>2</sub>O increased from 0–2%, 5% and 8%, the mercury removal efficiency decreased to 88.2%, 86.3 and 83.1%, respectively, which

demonstrated that  $\text{H}_2\text{O}$  was unfavorable for the removal of  $\text{Hg}^0$ . The mechanism of such inhibition effect was similar to that of  $\text{SO}_2$ . During the mercury removal, the competitive adsorption occurred between  $\text{H}_2\text{O}$  and  $\text{Hg}^0$ .  $\text{H}_2\text{O}$  vapor was adsorbed on the active sites of the adsorbent, thereby hindering the interface reaction between  $\text{Hg}^0$  and the active sites (Li et al. 2017b).

### 3.3 Regeneration performance test

In the actual production, if the deactivated adsorbent can be regenerated and reused by a facile regeneration method, the operating cost of mercury removal from coal-fired flue gas will be greatly reduced. In general,  $\text{Hg}^0$  is oxidized to  $\text{HgO}$  through  $\text{O}_A$  and  $\text{O}_B$  over the surface, which causes the active sites to be covered gradually with increasing  $\text{HgO}$  and eventually leads to deactivation of the adsorbent (Liao et al. 2016). The thermal treatment at high temperature has been proved to be a simple and effective method for mercury desorption and regeneration of active adsorption sites (Yang et al. 2015). The mercury and its oxides are desorbed and decomposed by high temperature heating, and the oxygen vacancies are supplemented by gas-phase oxygen to obtain regenerated adsorbents (Zhou & Diao 2020). Therefore, we achieved the regeneration of the deactivated adsorbent by desorption at  $400^\circ\text{C}$  for 1 hour in the  $\text{N}_2$  atmosphere and then heating at  $200^\circ\text{C}$  for 30 minutes in an air atmosphere. As displayed in Fig. 11a, the mercury removal efficiency after 5 cycles was reduced by approximately 2.3% compared with the original adsorbent. Moreover, the decrease in saturation magnetization before and after the cycles was negligible (Fig. 11b). These phenomena demonstrated that the as-prepared adsorbent possessed excellent regeneration performance, which can accomplish the regeneration and recycling of the deactivated adsorbent.

## 4. Conclusion

In summary, we successfully fabricated  $\text{Mn}_x\text{Cu}_y\text{-MATP}$  by co-precipitation and ultrasonic impregnation methods and utilized to remove  $\text{Hg}^0$  from coal-fired flue gas. BET, SEM, XRD, VSM and XPS were employed to systematically analyse the physicochemical properties of the as-prepared adsorbents. The effects of manganese and copper additions, reaction temperature and various components in the flue gas on the efficiency of  $\text{Hg}^0$  removal were investigated by the fixed-bed system. The results demonstrated that 8% Mn loading had reached the optimal mercury removal performance. The introduction of 5% Cu facilitated the dispersion of manganese oxides and the oxidation of  $\text{Hg}^0$ , however, excessive Cu can cause the accumulation of active components. The efficiency of mercury removal can be effectively promoted by NO and HCl with or without  $\text{O}_2$ , because the  $\text{NO}^+$ ,  $\text{NO}_3$ ,  $\text{NO}_2$  and  $\text{Cl}^*$  produced during the reaction can facilitate the adsorption and oxidation of  $\text{Hg}^0$ .  $\text{SO}_2$  and  $\text{H}_2\text{O}$  inhibited the oxidation of  $\text{Hg}^0$  owing to the competitive adsorption at the active sites. Moreover, the pores can be blocked by the sulfite and sulfate formed through  $\text{SO}_2$  and metal oxides. Interestingly, the introduction of Cu caused the sample to obtain  $\text{SO}_2$  resistance, which resulted in the mercury removal efficiency of 84.3% even under 1500 ppm  $\text{SO}_2$ . In addition, the mercury removal efficiency after 5 cycles was reduced by only 2.3% compared with the original adsorbent, denoting excellent regeneration performance. This paper provides a reference for

the development of mercury removal adsorbents with SO<sub>2</sub> resistance. Further studies to investigate the mechanism of SO<sub>2</sub> resistance are warranted.

## 5. Declarations

### Acknowledgements

The authors would like to thank for the support from Test Center of Wuhan University.

### Authors' contributions

All authors contributed to the study conception and design. Material preparation, data collection and analysis were performed by Yifei Long and Zhong He. The first draft of the manuscript was written by Yifei Long. Zhong He, Xiaoyi Li, Yajie Yin, Yuan Wang, Honghu Li and Jiangjun Hu commented on previous versions of the manuscript. All authors read and approved the final manuscript.

### Availability of data and materials

All data generated or analyzed during this study are included in this published article.

**Ethics approval and consent to participate** Not applicable.

**Consent for publication** Not applicable.

**Competing interest** The authors declare no competing interests.

## 6. References

1. Bao H, Zhang Z, Hua Q, Huang W (2014): Compositions, structures, and catalytic activities of CeO<sub>2</sub>@Cu<sub>2</sub>O nanocomposites prepared by the template-assisted method. *Langmuir* 30, 6427-6436
2. Borderieux S, Wu C-Y, Bonzongo J-C, Powers K (2004): control of elemental mercury vapor in combustion systems using Fe<sub>2</sub>O<sub>3</sub> nanoparticles. *Aerosol and Air Quality Research* 4, 74-90
3. Cao H, Li X, Chen Y, Gong M, Wang J (2012): Effect of loading content of copper oxides on performance of Mn-Cu mixed oxide catalysts for catalytic combustion of benzene. *Journal of Rare Earths* 30, 871-877
4. Chen C, Duan Y, Zhao S, Hu B, Li N, Yao T, Zhao Y, Wei H, Ren S (2019): Experimental study on mercury removal and regeneration of SO<sub>2</sub> modified activated carbon. *Industrial & Engineering Chemistry Research* 58, 13190-13197
5. Chen G, Zhang D, Zhang A, Zhang Z, Liu Z, Hou La (2017): CrO<sub>x</sub>-MnO<sub>x</sub>-TiO<sub>2</sub> adsorbent with high resistance to SO<sub>2</sub> poisoning for Hg<sup>0</sup> removal at low temperature. *Journal of Industrial and Engineering Chemistry* 55, 119-127

6. Chen J, Li C, Li S, Lu P, Gao L, Du X, Yi Y (2018): Simultaneous removal of HCHO and elemental mercury from flue gas over Co-Ce oxides supported on activated coke impregnated by sulfuric acid. *Chemical Engineering Journal* 338, 358-368
7. Chen W, Zhang Z, Bao W, Lai Y, Li J, Gan Y, Wang J (2014): Hierarchical mesoporous  $\gamma$ -Fe<sub>2</sub>O<sub>3</sub>/carbon nanocomposites derived from metal organic frameworks as a cathode electrocatalyst for rechargeable Li-O<sub>2</sub> batteries. *Electrochimica Acta* 134, 293-301
8. Ding F, Zhao Y, Mi L, Li H, Li Y, Zhang J (2012): Removal of gas-phase elemental mercury in flue gas by inorganic chemically promoted natural mineral sorbents. *Industrial & Engineering Chemistry Research* 51, 3039-3047
9. Dong J, Xu Z, Kuznicki SM (2009): Mercury removal from flue gases by novel regenerable magnetic nanocomposite sorbents. *Environ Sci Technol* 43, 3266-71
10. Dong L, Huang Y, Chen H, Liu L, Liu C, Xu L, Zha J, Wang Y, Liu H (2019): Magnetic  $\gamma$ -Fe<sub>2</sub>O<sub>3</sub>-loaded attapulgite sorbent for Hg<sup>0</sup> removal in coal-fired flue gas. *Energy & Fuels* 33, 7522-7533
11. Dong L, Wang H, Huang Y, Chen H, Cheng H, Liu L, Xu L, Zha J, Yu M, Wang S, Duan Y (2021): Elemental mercury removal from coal-fired flue gas using recyclable magnetic Mn-Fe based attapulgite sorbent. *Chemical Engineering Journal* 407, 127182
12. Feng J, Hou Z-Y, Zhou X-Y, Zhang H-L, Cheng T-Q, Lin T, Chen Y-Q (2017): Low-temperature catalytic oxidation of toluene over Mn-Co-O/Ce<sub>0.65</sub>Zr<sub>0.35</sub>O<sub>2</sub> mixed oxide catalysts. *Chemical Papers* 72, 161-172
13. Hosseini SA, Niaei A, Salari D, Alvarez-Galvan MC, Fierro JLG (2014): Study of correlation between activity and structural properties of Cu-(Cr, Mn and Co)<sub>2</sub> nano mixed oxides in VOC combustion. *Ceramics International* 40, 6157-6163
14. Hou W, Zhou J, Qi P, Gao X, Luo Z (2014): Effect of H<sub>2</sub>S/HCl on the removal of elemental mercury in syngas over CeO<sub>2</sub>-TiO<sub>2</sub>. *Chemical Engineering Journal* 241, 131-137
15. Huang T, Duan Y, Luo Z, Zhao S, Geng X, Xu Y, Huang Y, Wei H, Ren S, Wang H, Gu X (2019): Influence of flue gas conditions on mercury removal by activated carbon injection in a pilot-scale circulating fluidized bed combustion system. *Industrial & Engineering Chemistry Research* 58, 15553-15561
16. Jia T, Wu J, Song J, Liu Q, Wang J, Qi Y, He P, Qi X, Yang L, Zhao P (2020): In situ self-growing 3D hierarchical BiOBr/BiOI/O<sub>3</sub> Z-scheme heterojunction with rich oxygen vacancies and iodine ions as carriers transfer dual-channels for enhanced photocatalytic activity. *Chemical Engineering Journal* 396, 125258
17. Kim SC, Park Y-K, Nah JW (2014): Property of a highly active bimetallic catalyst based on a supported manganese oxide for the complete oxidation of toluene. *Powder Technology* 266, 292-298
18. Li H, Wu CY, Li Y, Zhang J (2011): CeO<sub>2</sub>-TiO<sub>2</sub> catalysts for catalytic oxidation of elemental mercury in low-rank coal combustion flue gas. *Environ Sci Technol* 45, 7394-400
19. Li H, Wu CY, Li Y, Li L, Zhao Y, Zhang J (2012): Role of flue gas components in mercury oxidation over TiO<sub>2</sub> supported MnO<sub>x</sub>-CeO<sub>2</sub> mixed-oxide at low temperature. *J Hazard Mater* 243, 117-23

20. Li H, Wang S, Wang X, Tang N, Pan S, Hu J (2017a): Catalytic oxidation of  $\text{Hg}^0$  in flue gas over Ce modified  $\text{TiO}_2$  supported Co-Mn catalysts: Characterization, the effect of gas composition and co-benefit of NO conversion. *Fuel* 202, 470-482
21. Li H, Wang S, Wang X, Tang N, Pan S, Hu J (2017b): Catalytic oxidation of  $\text{Hg}^0$  in flue gas over Ce modified  $\text{TiO}_2$  supported Co-Mn catalysts: Characterization, the effect of gas composition and co-benefit of NO conversion. *Fuel* 202, 470-482
22. Li M, Wang L, Chen J-y, Jiang Y-l, Wang W-j (2014): Adsorption performance and mechanism of bentonite modified by ammonium bromide for gas-phase elemental mercury removal. *Journal of Fuel Chemistry and Technology* 42, 1266-1272
23. Liao Y, Chen D, Zou S, Xiong S, Xiao X, Dang H, Chen T, Yang S (2016): Recyclable naturally derived magnetic pyrrhotite for elemental mercury recovery from flue gas. *Environ Sci Technol* 50, 10562-10569
24. Liu F, Zhang J, Zhao Y, Zheng C (2014): Mercury removal from flue gas by metal oxide-loaded attapulgite mineral sorbent. *Journal of Combustion Science and Technology* 20, 553-557
25. Liu H, Yang J, Tian C, Zhao Y, Zhang J (2017): Mercury removal from coal combustion flue gas by modified palygorskite adsorbents. *Applied Clay Science* 147, 36-43
26. Liu H, Chang L, Liu W, Xiong Z, Zhao Y, Zhang J (2020): Advances in mercury removal from coal-fired flue gas by mineral adsorbents. *Chemical Engineering Journal* 379, 122263
27. Liu P, Wei G, Liang X, Chen D, He H, Chen T, Xi Y, Chen H, Han D, Zhu J (2018): Synergetic effect of Cu and Mn oxides supported on palygorskite for the catalytic oxidation of formaldehyde: Dispersion, microstructure, and catalytic performance. *Applied Clay Science* 161, 265-273
28. Shan Y, Yang W, Li Y, Liu Y, Pan J (2019): Preparation of microwave-activated magnetic bio-char adsorbent and study on removal of elemental mercury from flue gas. *The Science of the total environment* 697, 134049
29. Shao H, Liu X, Zhou Z, Zhao B, Chen Z, Xu M (2016): Elemental mercury removal using a novel KI modified bentonite supported by starch sorbent. *Chemical Engineering Journal* 291, 306-316
30. Tao S, Li C, Fan X, Zeng G, Lu P, Zhang X, Wen Q, Zhao W, Luo D, Fan C (2012): Activated coke impregnated with cerium chloride used for elemental mercury removal from simulated flue gas. *Chemical Engineering Journal* 210, 547-556
31. Wang Y, Li C, Zhao L, Xie Y, Zhang X, Zeng G, Wu H, Zhang J (2016): Study on the removal of elemental mercury from simulated flue gas by  $\text{Fe}_2\text{O}_3\text{-CeO}_2/\text{AC}$  at low temperature. *Environmental science and pollution research international* 23, 5099-110
32. Wang Y, Li H, Wang S, Wang X, He Z, Hu J (2019a): Investigation of sulphated  $\text{CuCl}_2/\text{TiO}_2$  catalyst for simultaneous removal of  $\text{Hg}^0$  and NO in SCR process. *Fuel Processing Technology* 188, 179-189
33. Wang Y, Yang D, Li S, Zhang L, Zheng G, Guo L (2019b): Layered copper manganese oxide for the efficient catalytic CO and VOCs oxidation. *Chemical Engineering Journal* 357, 258-268

34. Wang Y, Li H, He Z, Zhang M, Guan J, Qian K, Xu J, Hu J (2020): Removal of elemental mercury from flue gas using the magnetic Fe-containing carbon prepared from the sludge flocculated with ferrous sulfate. *Environmental science and pollution research international* 27, 30254-30264
35. Wilcox J, Rupp E, Ying SC, Lim D-H, Negreira AS, Kirchofer A, Feng F, Lee K (2012): Mercury adsorption and oxidation in coal combustion and gasification processes. *International Journal of Coal Geology* 90-91, 4-20
36. Wu J, Zhao Z, Huang T, Sheng P, Zhang J, Tian H, Zhao X, Zhao L, He P, Ren J, Gao K (2017): Removal of elemental mercury by Ce-Mn co-modified activated carbon catalyst. *Catalysis Communications* 93, 62-66
37. Xu H, Yan N, Qu Z, Liu W, Mei J, Huang W, Zhao S (2017): Gaseous heterogeneous catalytic reactions over Mn-based oxides for environmental applications: a critical review. *Environ Sci Technol* 51, 8879-8892
38. Xu W, Wang H, Zhou X, Zhu T (2014): CuO/TiO<sub>2</sub> catalysts for gas-phase Hg<sup>0</sup> catalytic oxidation. *Chemical Engineering Journal* 243, 380-385
39. Xu Y, Luo G, Pang Q, He S, Deng F, Xu Y, Yao H (2019): Adsorption and catalytic oxidation of elemental mercury over regenerable magnetic Fe-Ce mixed oxides modified by non-thermal plasma treatment. *Chemical Engineering Journal* 358, 1454-1463
40. Yang J, Zhao Y, Chang L, Zhang J, Zheng C (2015): Mercury adsorption and oxidation over cobalt oxide loaded magnetospheres catalyst from fly ash in oxyfuel combustion flue gas. *Environ Sci Technol* 49, 8210-8
41. Yang J, Zhao Y, Liang S, Zhang S, Ma S, Li H, Zhang J, Zheng C (2018a): Magnetic iron–manganese binary oxide supported on carbon nanofiber (Fe<sub>3-x</sub>Mn<sub>x</sub>O<sub>4</sub>/CNF) for efficient removal of Hg<sup>0</sup> from coal combustion flue gas. *Chemical Engineering Journal* 334, 216-224
42. Yang J, Zhu W, Qu W, Yang Z, Wang J, Zhang M, Li H (2019a): Selenium functionalized metal-organic framework MIL-101 for efficient and permanent sequestration of mercury. *Environ Sci Technol* 53, 2260-2268
43. Yang J, Zhu W, Zhang S, Zhang M, Qu W, Li H, Zeng Z, Zhao Y, Zhang J (2019b): Role of flue gas components in Hg<sup>0</sup> oxidation over La<sub>0.8</sub>Ce<sub>0.2</sub>MnO<sub>3</sub> perovskite catalyst in coal combustion flue gas. *Chemical Engineering Journal* 360, 1656-1666
44. Yang R, Mei C, Wu X, Yu X, Shi Z (2019c): Mn–Cu binary metal oxides with molecular-scale homogeneity for Hg<sup>0</sup> removal from coal-fired flue gas. *Industrial & Engineering Chemistry Research* 58, 19292-19301
45. Yang S, Yan N, Guo Y, Wu D, He H, Qu Z, Li J, Zhou Q, Jia J (2011): Gaseous elemental mercury capture from flue gas using magnetic nanosized (Fe<sub>3-x</sub>Mn<sub>x</sub>)<sub>1-δ</sub>O<sub>4</sub>. *Environ Sci Technol* 45, 1540-6
46. Yang W, Li Y, Shi S, Chen H, Shan Y, Liu Y (2019d): Mercury removal from flue gas by magnetic iron-copper oxide modified porous char derived from biomass materials. *Fuel* 256, 115977

47. Yang W, Chen H, Han X, Ding S, Shan Y, Liu Y (2020a): Preparation of magnetic Co-Fe modified porous carbon from agricultural wastes by microwave and steam activation for mercury removal. *J Hazard Mater* 381, 120981
48. Yang Y, Liu J, Wang Z (2020b): Reaction mechanisms and chemical kinetics of mercury transformation during coal combustion. *Progress in Energy and Combustion Science* 79, 100844
49. Yang Z, Li H, Liu X, Li P, Yang J, Lee P-H, Shih K (2018b): Promotional effect of CuO loading on the catalytic activity and SO<sub>2</sub> resistance of MnO<sub>x</sub>/TiO<sub>2</sub> catalyst for simultaneous NO reduction and Hg<sup>0</sup> oxidation. *Fuel* 227, 79-88
50. Yi H, Yang X, Tang X, Zhao S, Wang J, Cui X, Feng T, Ma Y (2017): Removal of toluene from industrial gas over 13X zeolite supported catalysts by adsorption-plasma catalytic process. *Journal of Chemical Technology & Biotechnology* 92, 2276-2286
51. Zhang H, Sun H, Zhao K, Han Y, Wu J, Jiao T, Liang P (2018): Influences of water vapor and fly ash on elemental mercury removal over cerium-oxide-modified semi-coke. *Fuel* 217, 211-217
52. Zhang J, Zhang L, Zhou S, Chen H, Zhong H, Zhao Y, Wang X (2014): Magnetically separable attapulgite-TiO<sub>2</sub>-FeO composites with superior activity towards photodegradation of methyl orange under visible light radiation. *Journal of Industrial and Engineering Chemistry* 20, 3884-3889
53. Zhang S, Zhao Y, Wang Z, Zhang J, Wang L, Zheng C (2017): Integrated removal of NO and mercury from coal combustion flue gas using manganese oxides supported on TiO<sub>2</sub>. *Journal of environmental sciences* 53, 141-150
54. Zhang Y, Li C, Zhu Y, Du X, Lyu Y, Li S, Zhai Y (2020): Insight into the enhanced performance of toluene removal from simulated flue gas over Mn-Cu oxides modified activated coke. *Fuel* 276, 118099
55. Zhang Z, Wu J, Li B, Xu H, Liu D (2019): Removal of elemental mercury from simulated flue gas by ZSM-5 modified with Mn-Fe mixed oxides. *Chemical Engineering Journal* 375, 121946
56. Zhao H, Mu X, Yang G, George M, Cao P, Fanady B, Rong S, Gao X, Wu T (2017): Graphene-like MoS<sub>2</sub> containing adsorbents for Hg<sup>0</sup> capture at coal-fired power plants. *Applied Energy* 207, 254-264
57. Zhao S, Pudasainee D, Duan Y, Gupta R, Liu M, Lu J (2019): A review on mercury in coal combustion process: Content and occurrence forms in coal, transformation, sampling methods, emission and control technologies. *Progress in Energy and Combustion Science* 73, 26-64
58. Zhou F, Diao Y (2020): Magnetic copper-ferrosilicon composites as regenerable sorbents for Hg<sup>0</sup> removal. *Colloids and Surfaces A: Physicochemical and Engineering Aspects* 590, 124447
59. Zhou Q, Tao X, Lei Y, Liu Y, Lu P, Wang Y (2019): Effect of molybdenum incorporation on the activity of a magnetic Fe-Mn sorbent for the capture of elemental mercury. *Energy & Fuels* 33, 2390-2398

## Figures

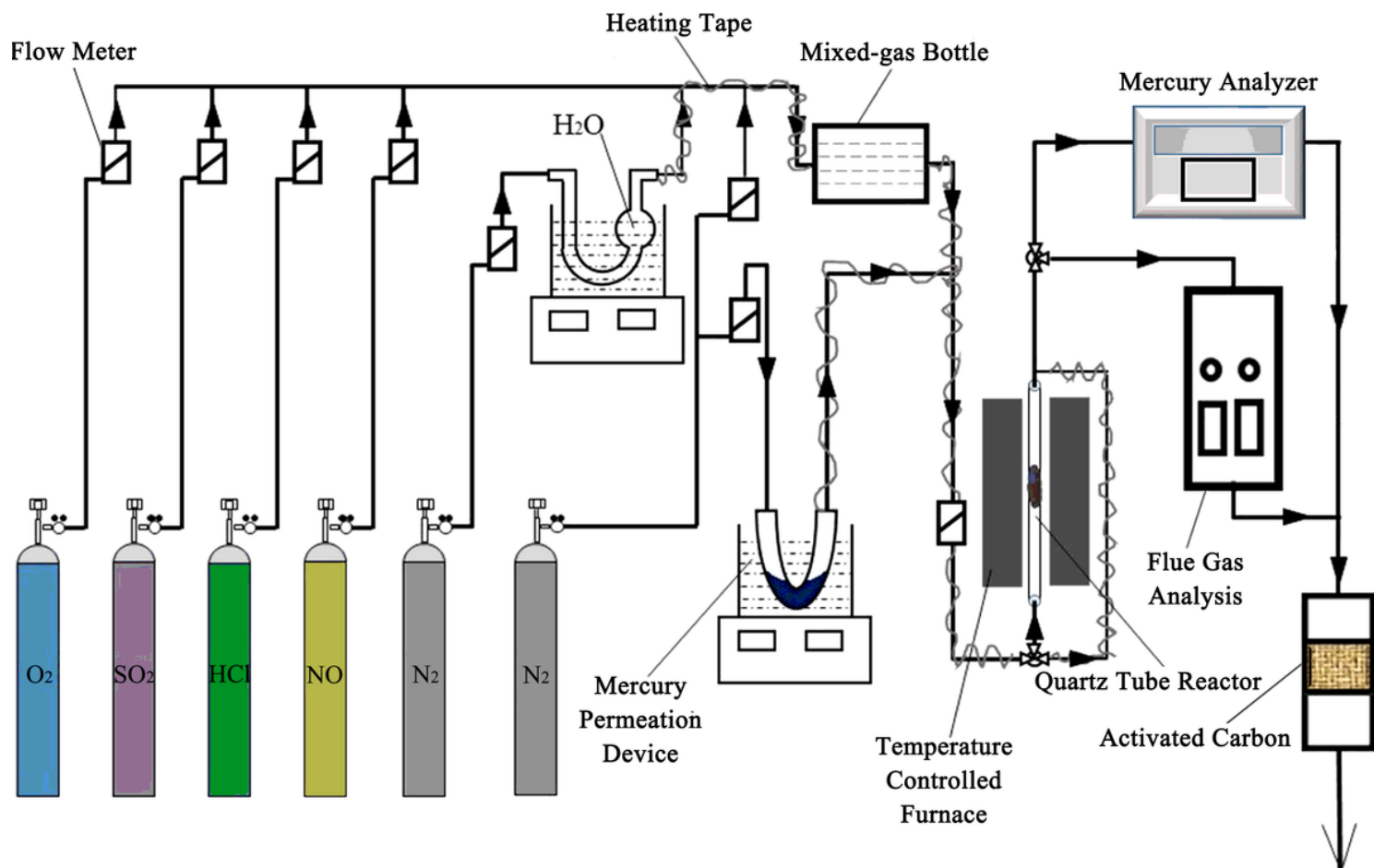


**Figure 1**

Schematic diagram of the experimental apparatus.

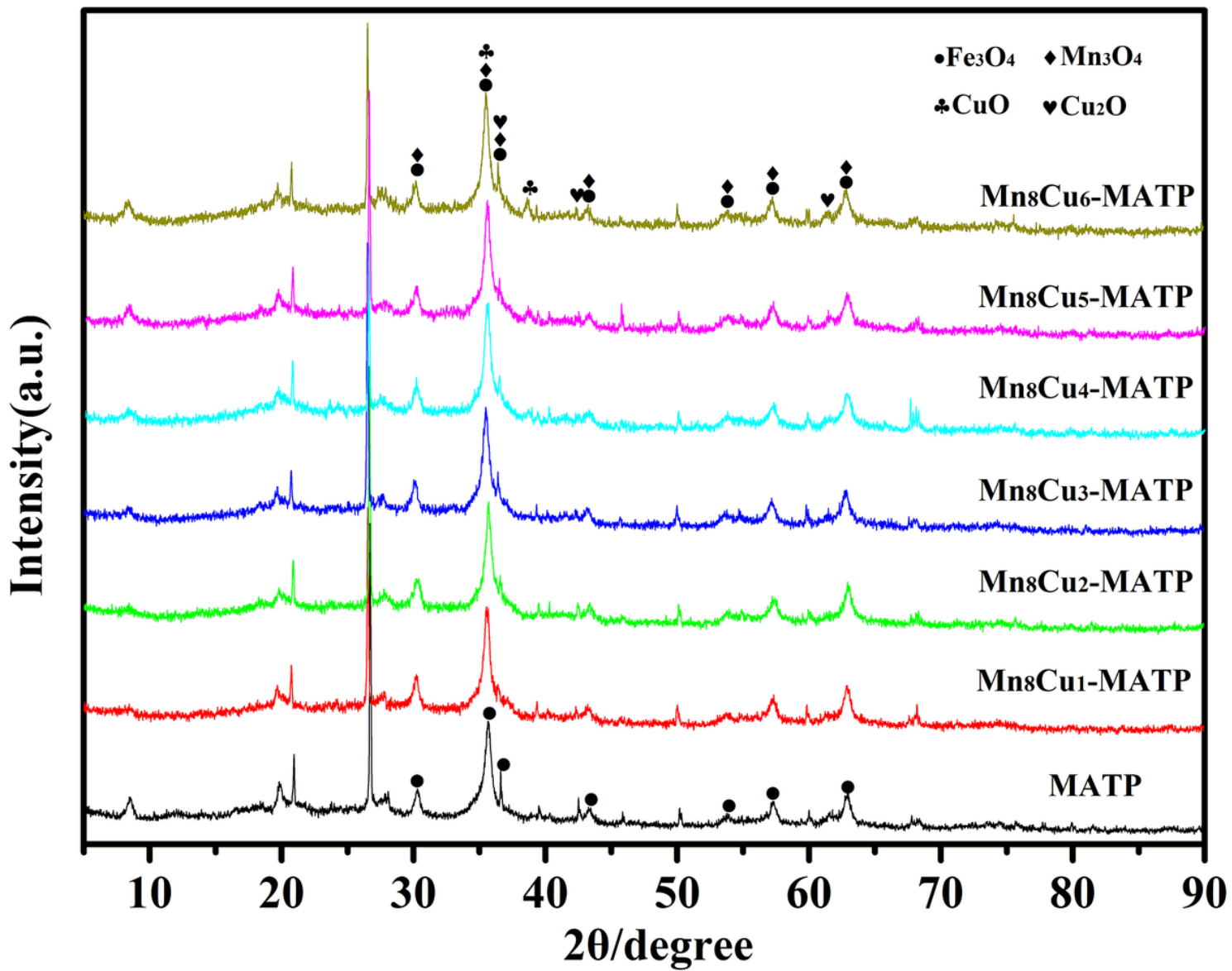
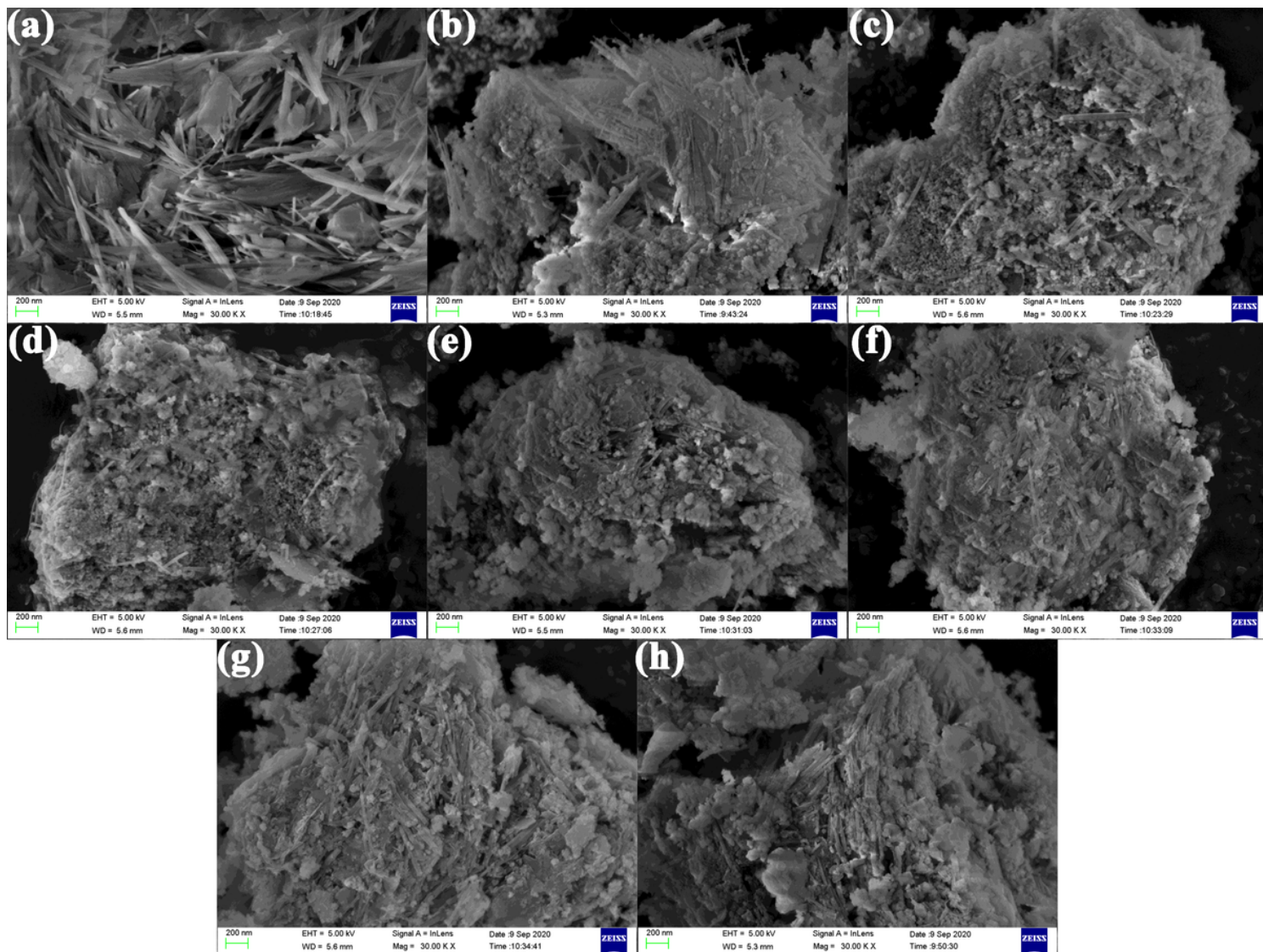


Figure 2

XRD patterns of MATP and Mn<sub>8</sub>Cu<sub>y</sub>-MATP samples.



**Figure 3**

SEM images of (a) the original ATP, (b) MATP, (c) Mn8Cu1-MATP, (d) Mn8Cu2-MATP, (e) Mn8Cu3-MATP, (f) Mn8Cu4-MATP, (g) Mn8Cu5-MATP and (h) Mn8Cu6-MATP.

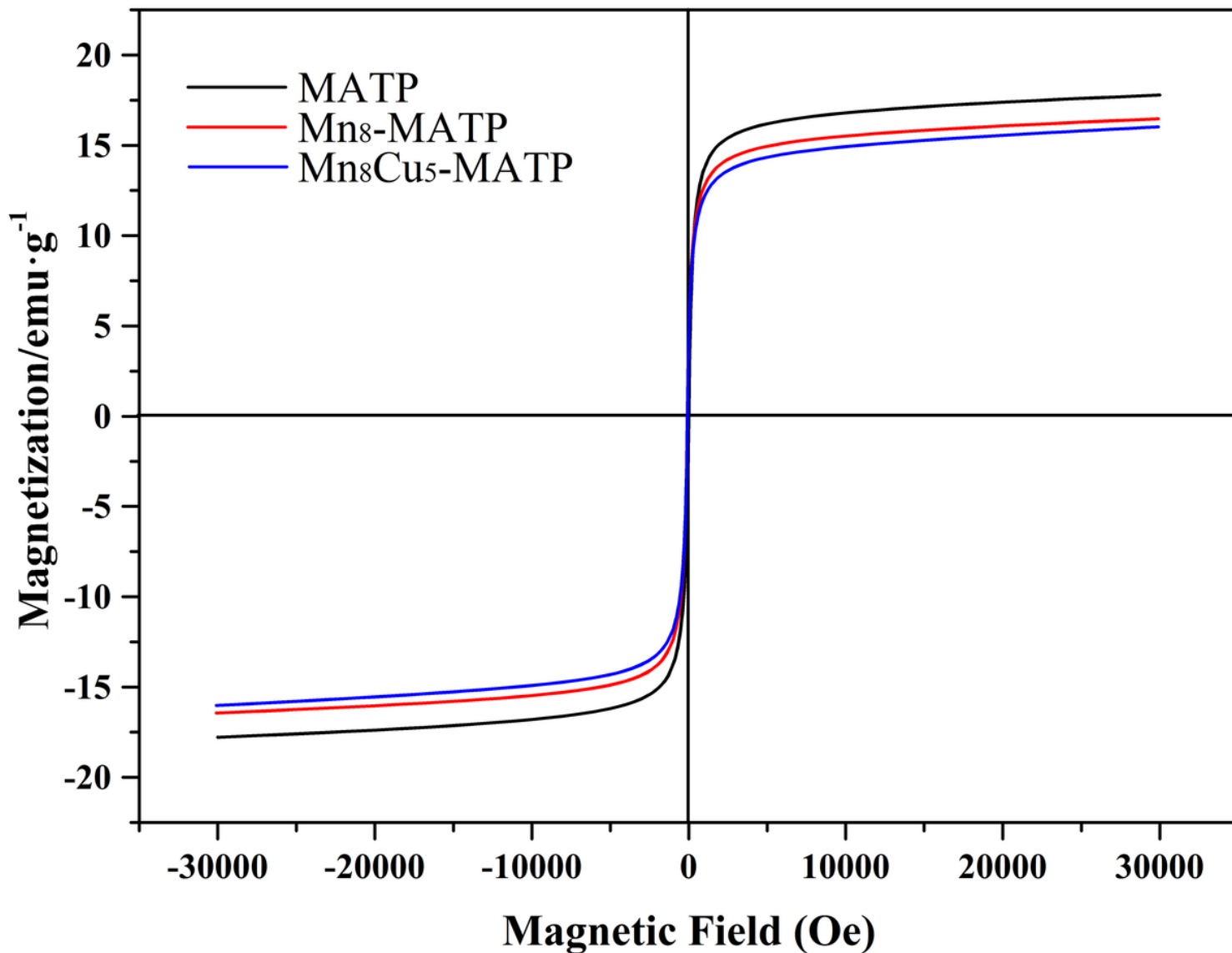
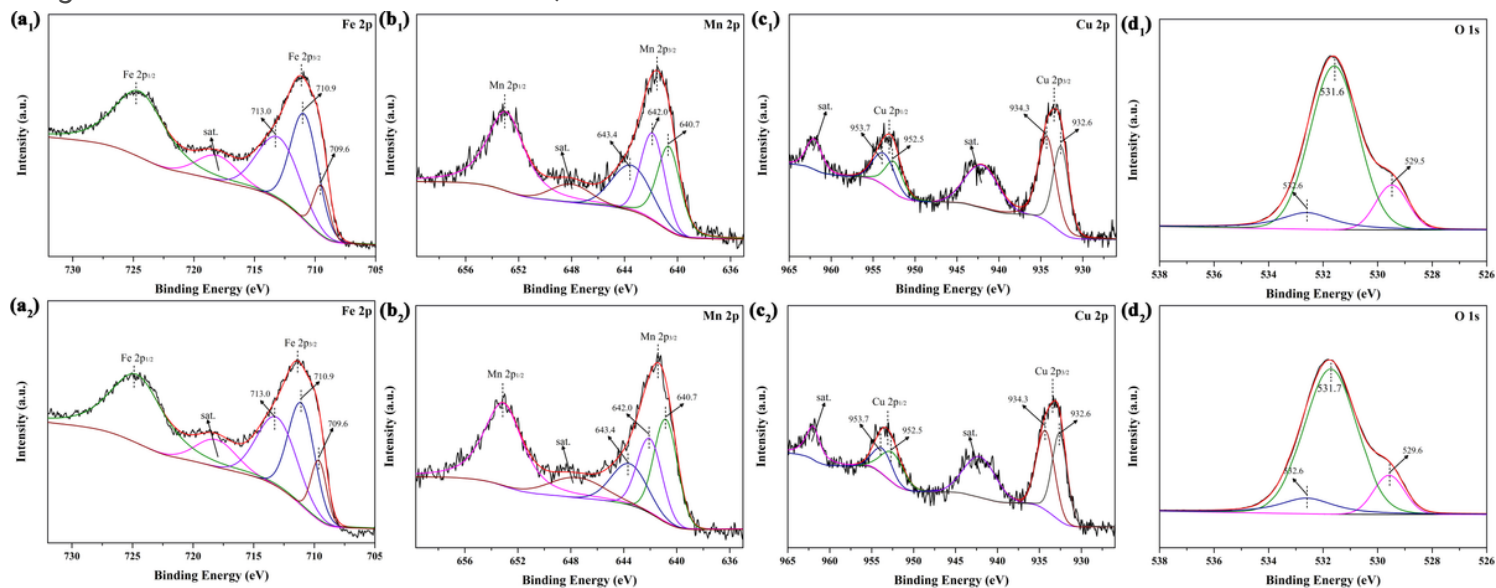


Figure 4

Magnetization characteristics of MATP, Mn<sub>8</sub>-MATP and Mn<sub>8</sub>Cu<sub>5</sub>-MATP.



**Figure 5**

XPS spectra of (a) Fe 2p, (b) Mn 2p, (c) Cu 2p, and (d) O 1s over the Mn<sub>8</sub>Cu<sub>5</sub>-MATP sample (1) before and (2) after mercury removal.

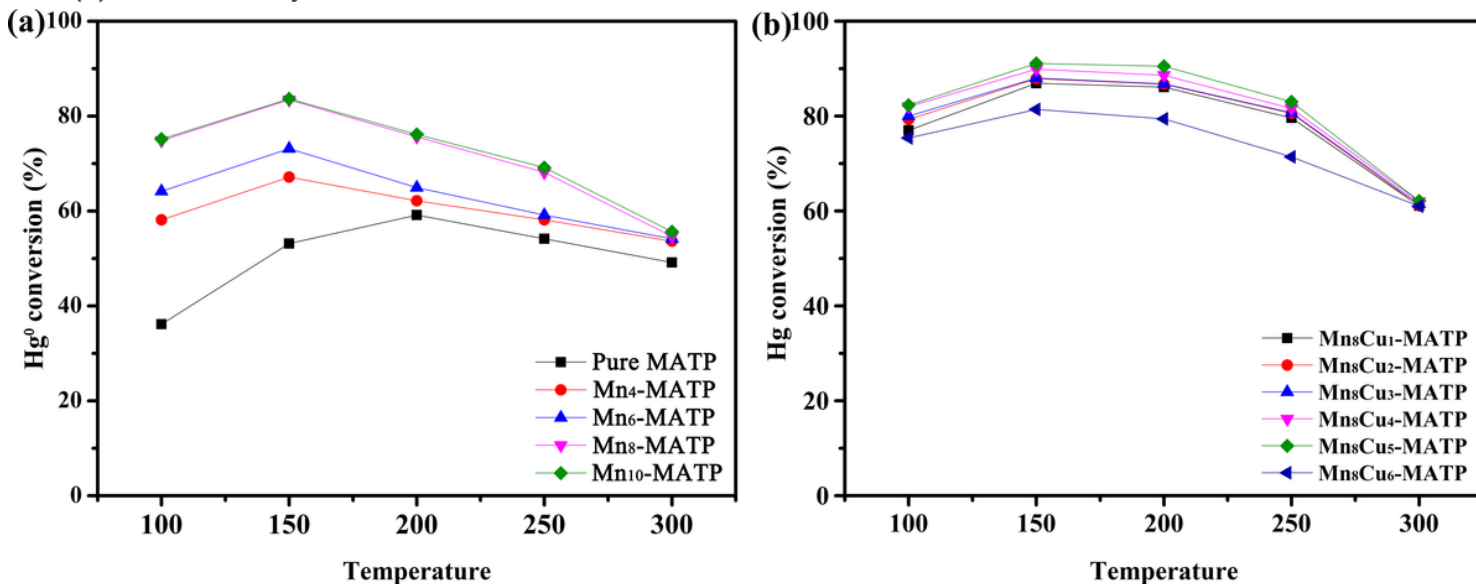


**Figure 6**

(a) Hg<sup>0</sup> conversion over different Mn loading on MATP samples in flue gas. (b) Hg<sup>0</sup> conversion over different Cu loading on Mn<sub>8</sub>-MATP samples in flue gas. (Reaction condition: 55 µg/m<sup>3</sup> Hg<sup>0</sup>, 6% O<sub>2</sub>, N<sub>2</sub> as balance gas, T=100-300 °C)

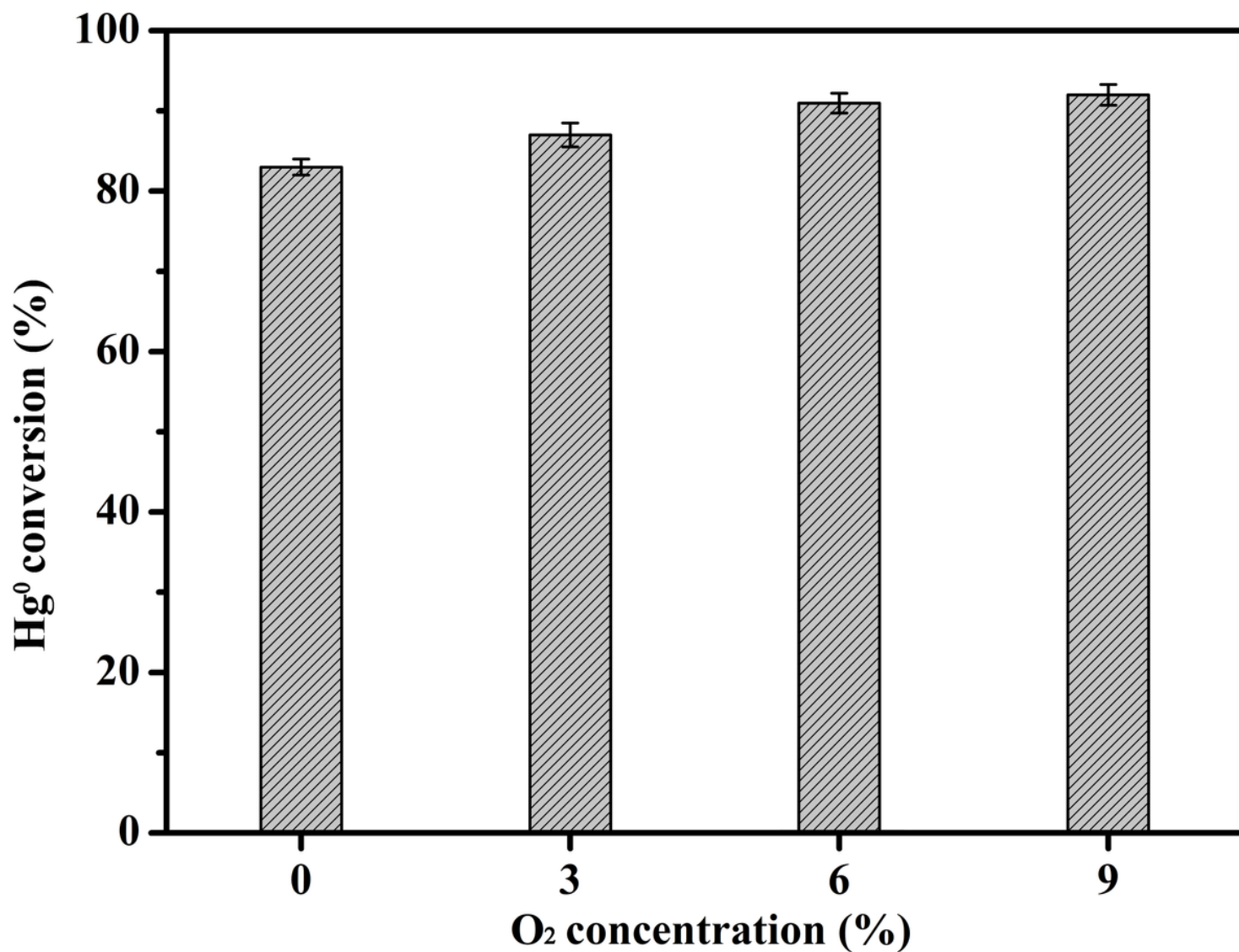


Figure 7

Effect of O<sub>2</sub> on Hg<sup>0</sup> removal efficiency of Mn<sub>8</sub>Cu<sub>5</sub>-MATP.

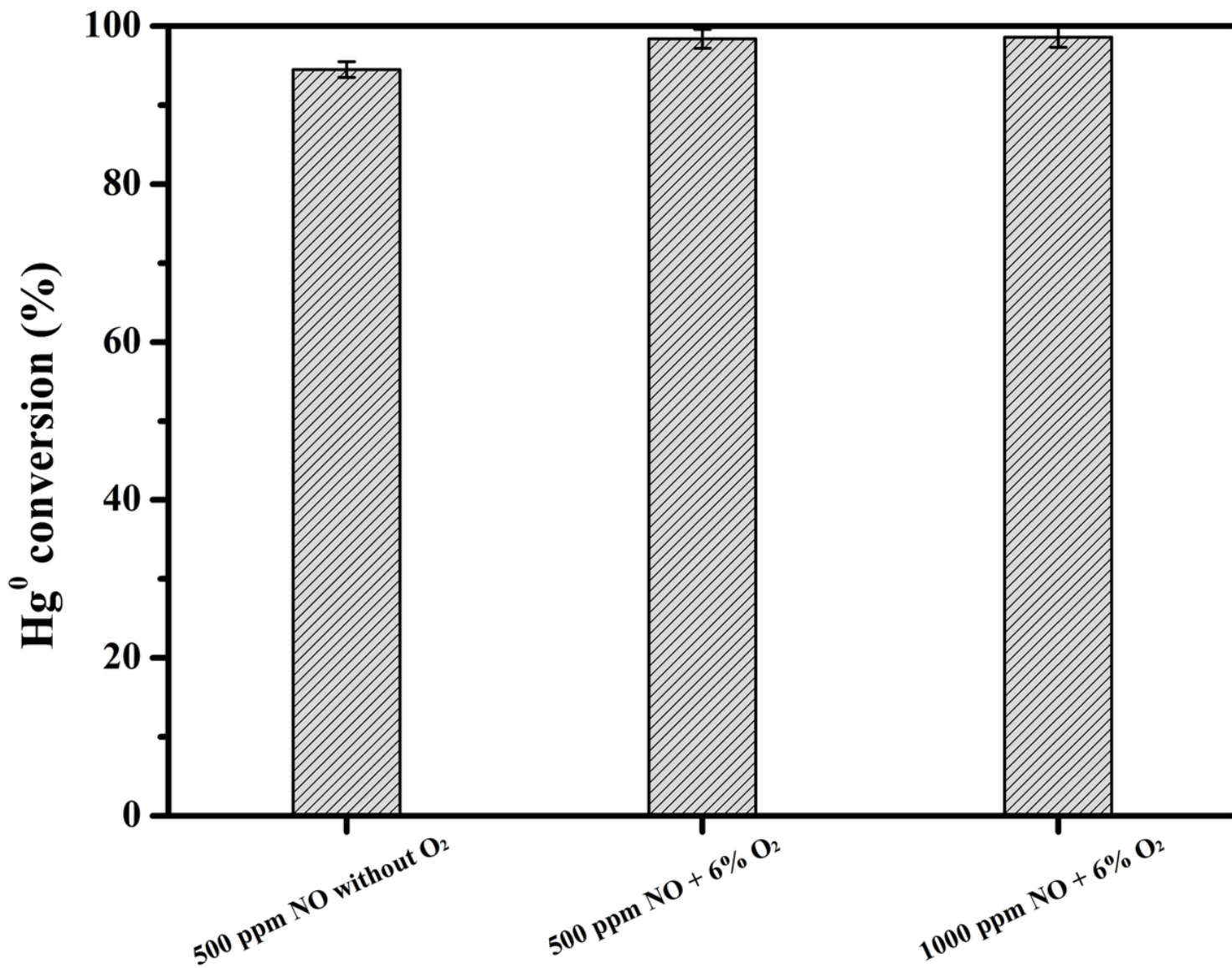


Figure 8

Effect of NO on Hg<sup>0</sup> removal efficiency of Mn<sub>8</sub>Cu<sub>5</sub>-MATP.

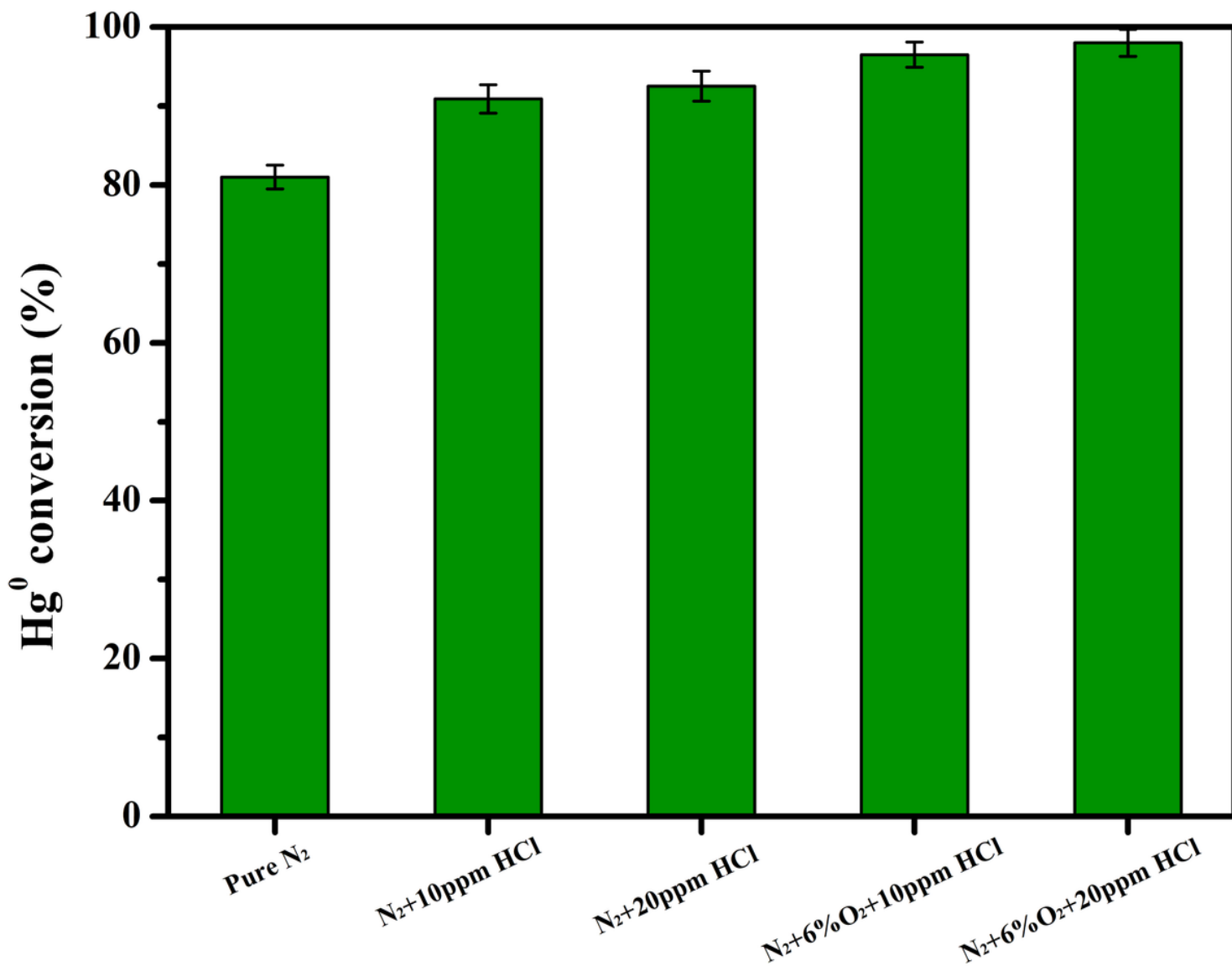
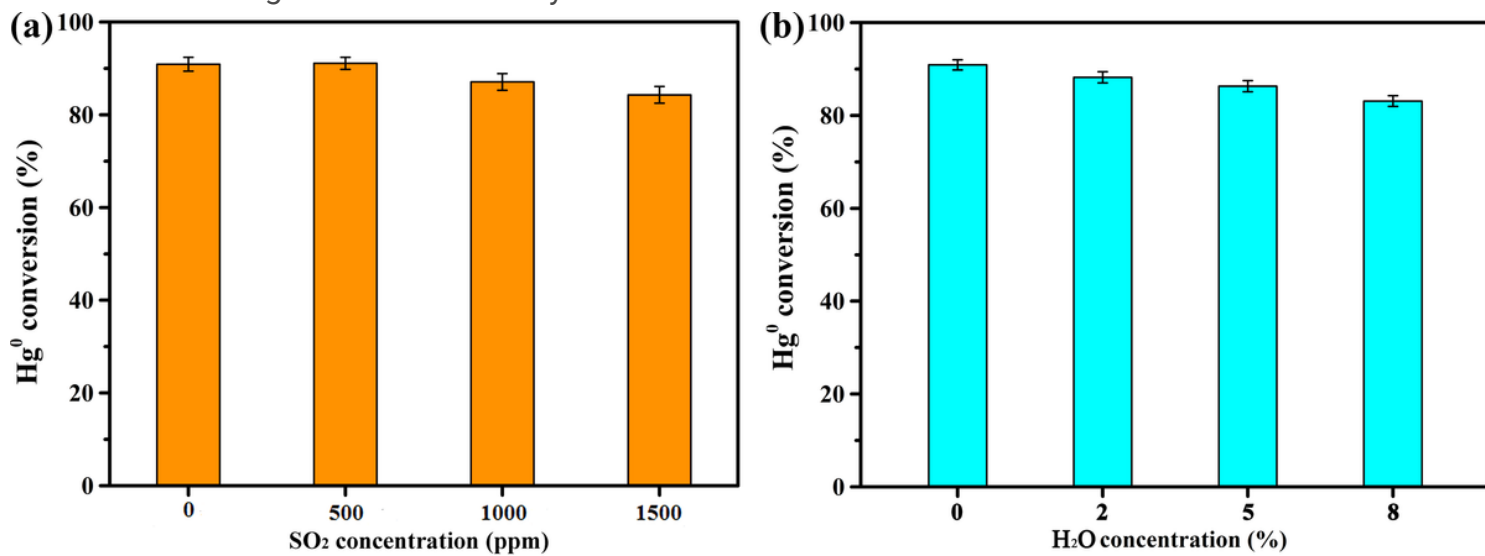


Figure 9

Effect of HCl on Hg<sup>0</sup> removal efficiency of Mn<sub>8</sub>Cu<sub>5</sub>-MATP.



**Figure 10**

Effect of (a) SO<sub>2</sub> and (b) H<sub>2</sub>O on Hg<sup>0</sup> removal efficiency of Mn<sub>8</sub>Cu<sub>5</sub>-MATP. 3.3.4. Effect of SO<sub>2</sub> and H<sub>2</sub>O

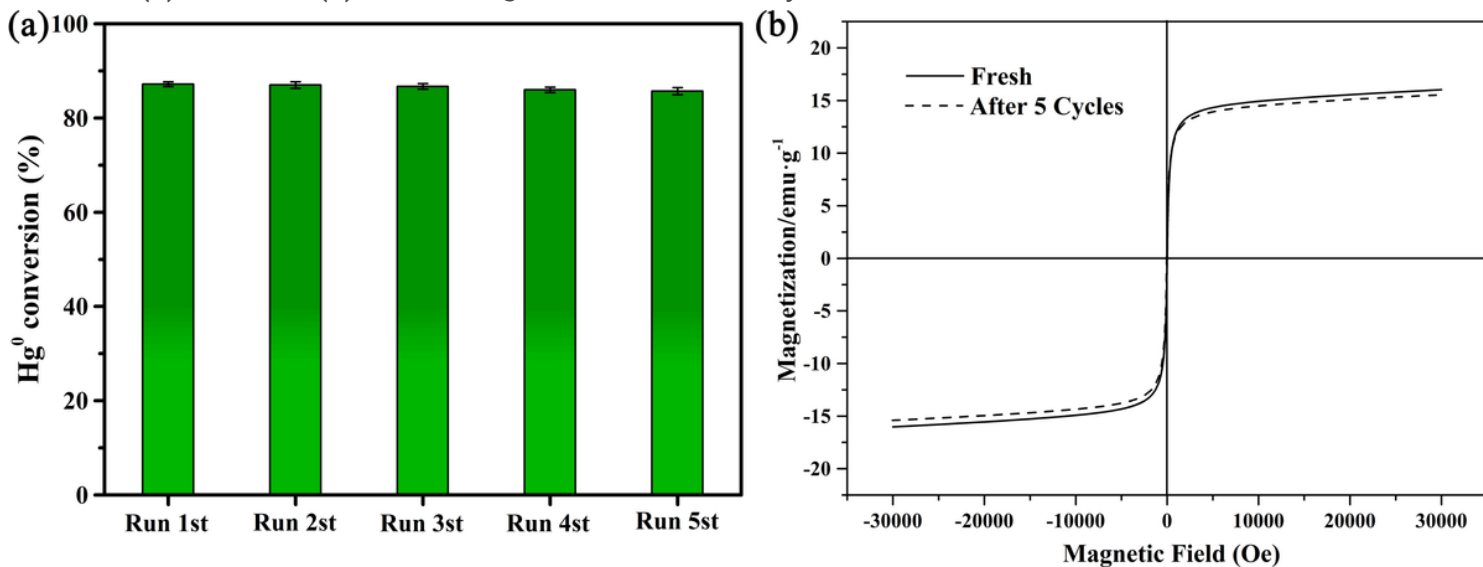


**Figure 11**

(a) Hg<sup>0</sup> removal performance of Mn<sub>8</sub>Cu<sub>5</sub>-MATP under five regeneration cycles. (b) Magnetization characteristics of fresh and regenerated Mn<sub>8</sub>Cu<sub>5</sub>-MATP